

Very early identification of a bimodal frictional behavior during the post-seismic phase of the 2015 M_w 8.3 Illapel, Chile, earthquake

Cedric Twardzik^{1,2}, Mathilde Vergnolle¹, Anthony Sladen¹, and Louisa L. H. Tsang^{1,3}

¹Université Côte d'Azur, CNRS, Observatoire de la Côte d'Azur, IRD, Geoazur, UMR7329, Valbonne, France

²now at: Institut de Physique du Globe de Strasbourg, UMR7516, Université de Strasbourg, EOST, CNRS, Strasbourg, France

³now at: University of Surrey, International Study Centre, Guildford, United Kingdom

Correspondence: Cedric Twardzik (twardzik@unistra.fr)

Contents

S1	Post-processing of the kinematic position time series	2
S2	Choice of the smoothing parameter	10
S3	Comparison between observed and calculated surface displacements	11
5 S4	Comparison between the post-seismic slip model and various co-seismic slip models	20
S5	Sensitivity analysis	22
S6	Comparison between very early post-seismic slip and very early aftershocks using Frank et al. (2017) catalog	26
S7	Comparison with the cumulative moment of aftershocks	29

S1 Post-processing of the kinematic position time series

10 The following figures (Figure S1.1 to S1.15) show the processing steps to obtain the hourly position time series used in this study. For each station, we show on the top row the raw position time series. The red dashed line indicates the time of the mainshock and the blue dashed lines the time of the two largest aftershock (see main text). The mean and a linear trend have been removed using the 6 days prior to the mainshock origin time. The co-seismic static offsets of the mainshock are also removed. The standard deviation of the time series is calculated using the 6 days prior to the mainshock. The second row shows the position time series after we apply a sidereal filter that is constructed as proposed by Twardzik et al. (2019). This allows the noise level to decrease by $\sim 35\%$ on average. The third row shows the hourly position time series used to obtain the post-seismic slip distribution over the first 12 hours (orange dots). Each position is obtained by computing the average position over a 1-hour long time window that is centered on the time of interest and that spans 30 minutes on either side. Finally, we show on the bottom row the hourly position time series after the 2 largest aftershocks are removed from the raw position time series. The figures are sorted from the northern to the southern stations.

15

20

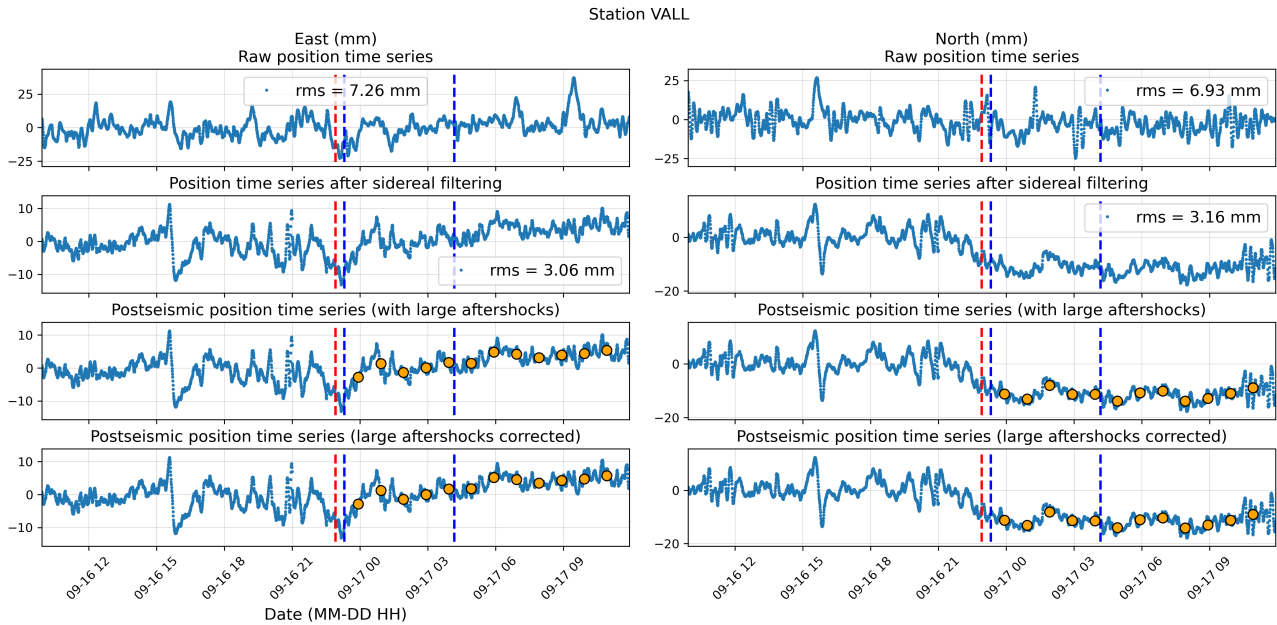


Figure S1.1.

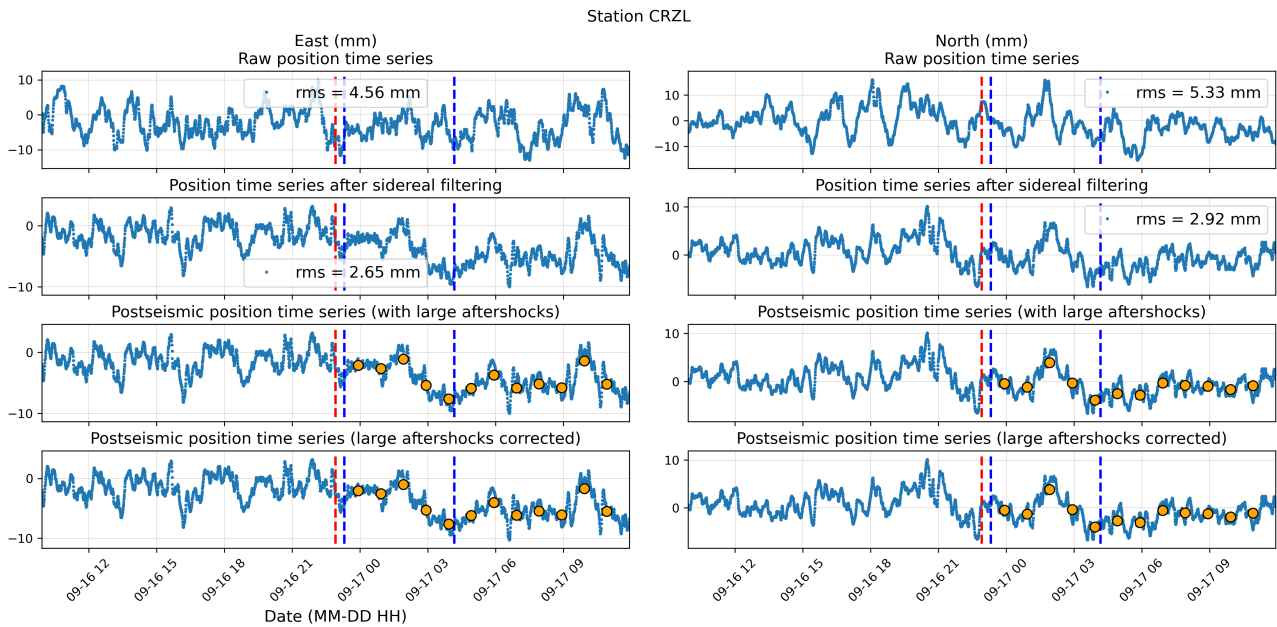


Figure S1.2.

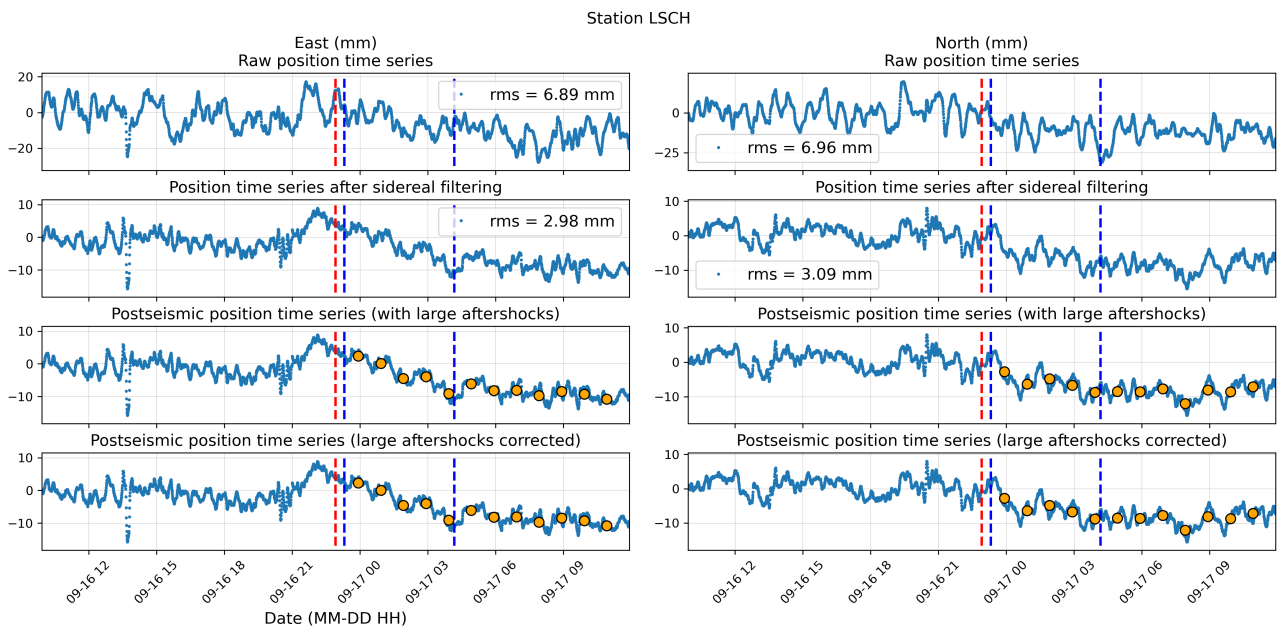


Figure S1.3.

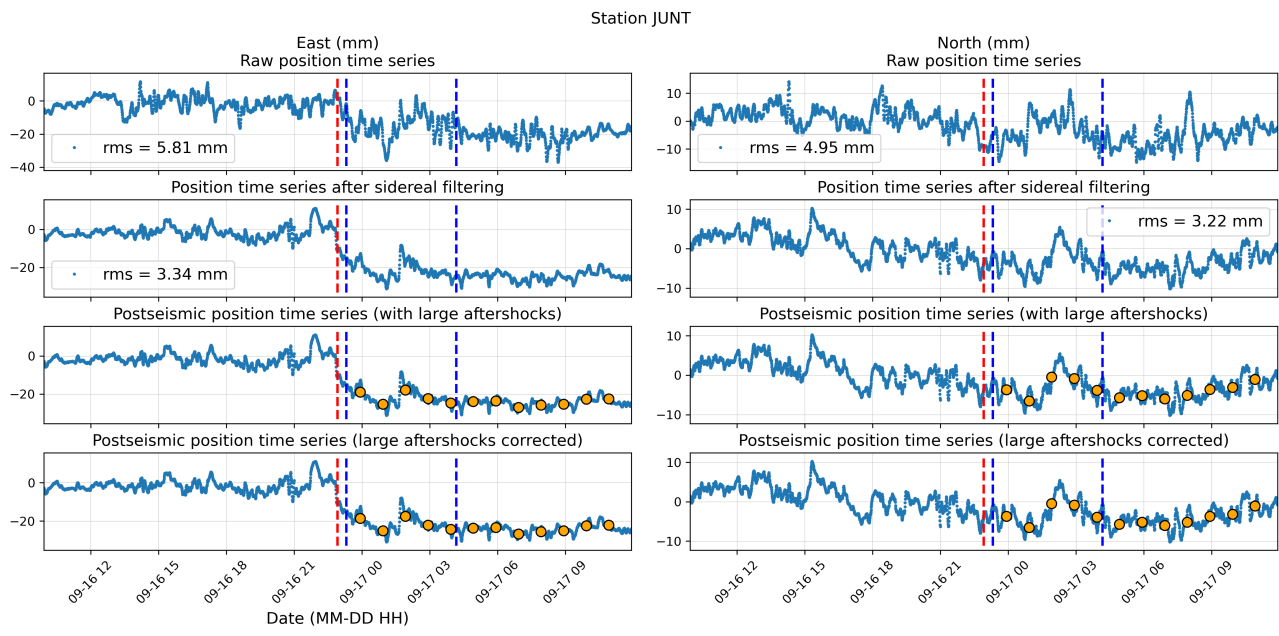


Figure S1.4.

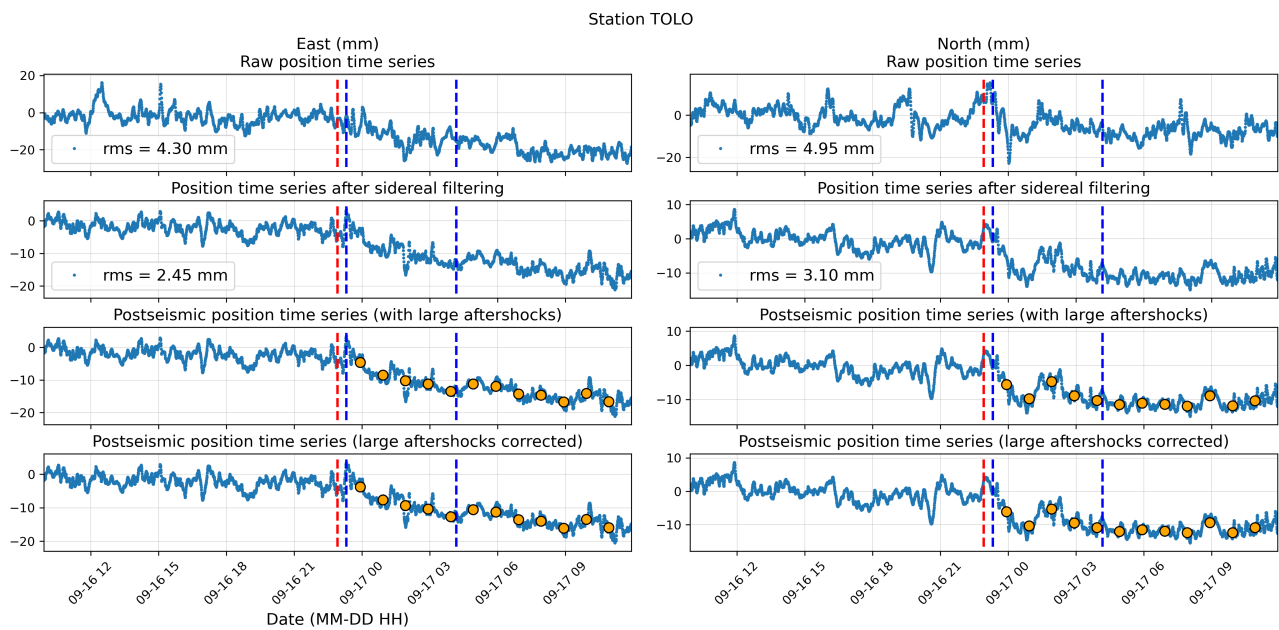


Figure S1.5.

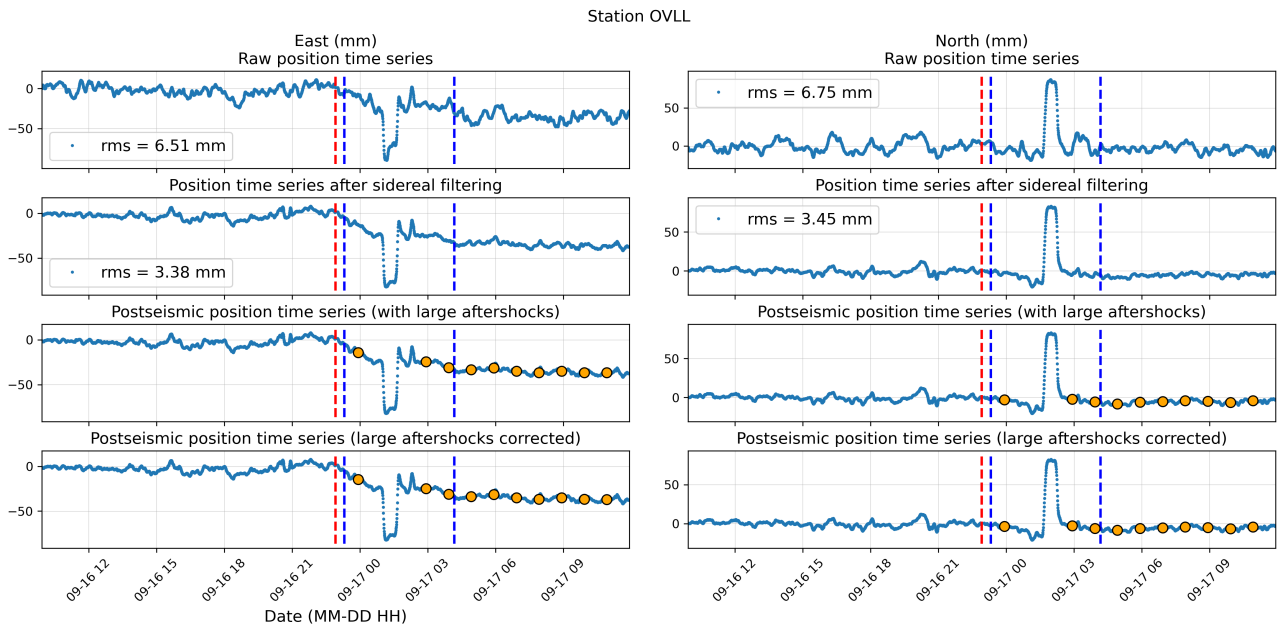


Figure S1.6.

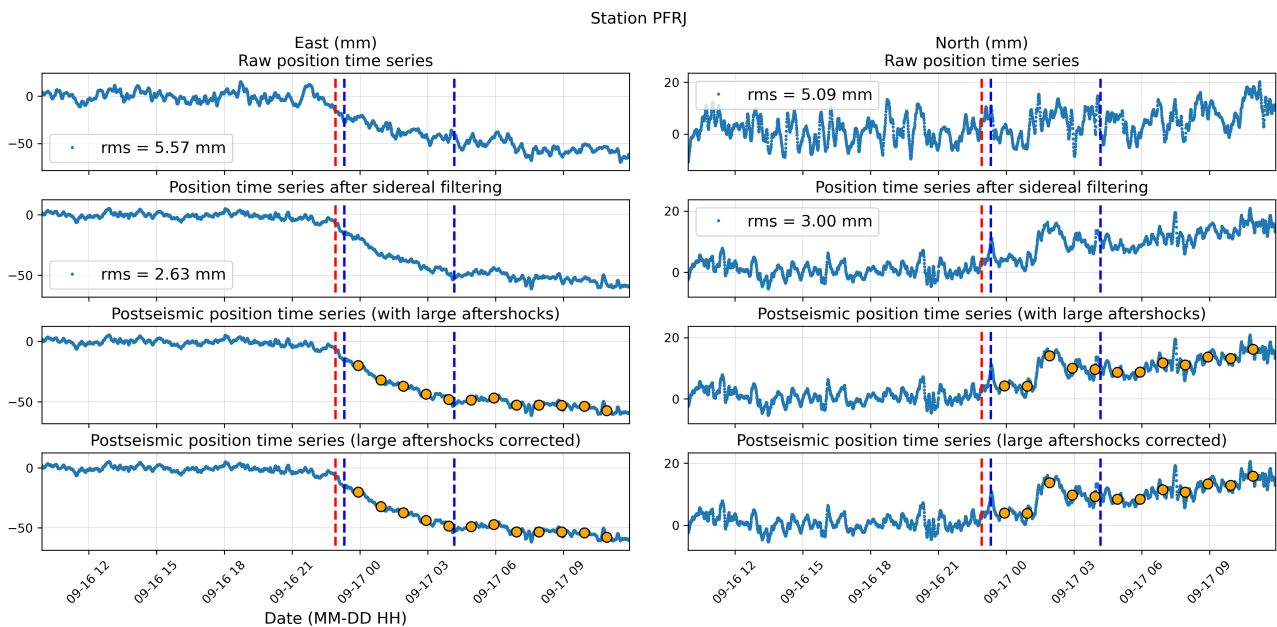


Figure S1.7.

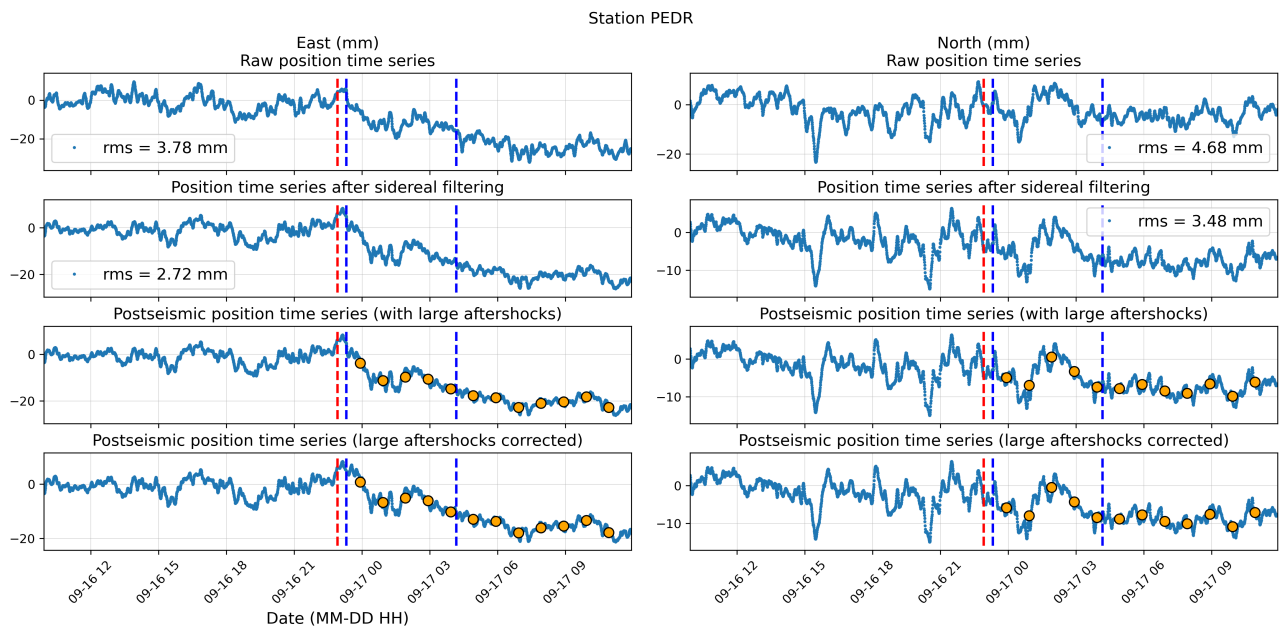


Figure S1.8.

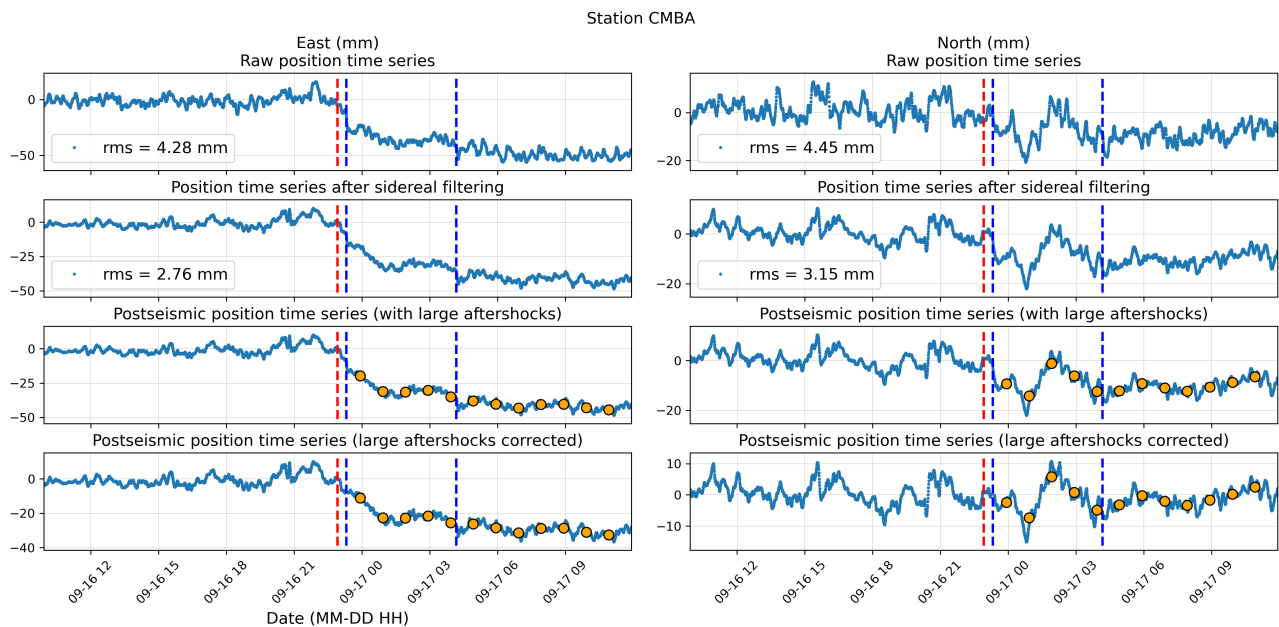


Figure S1.9.

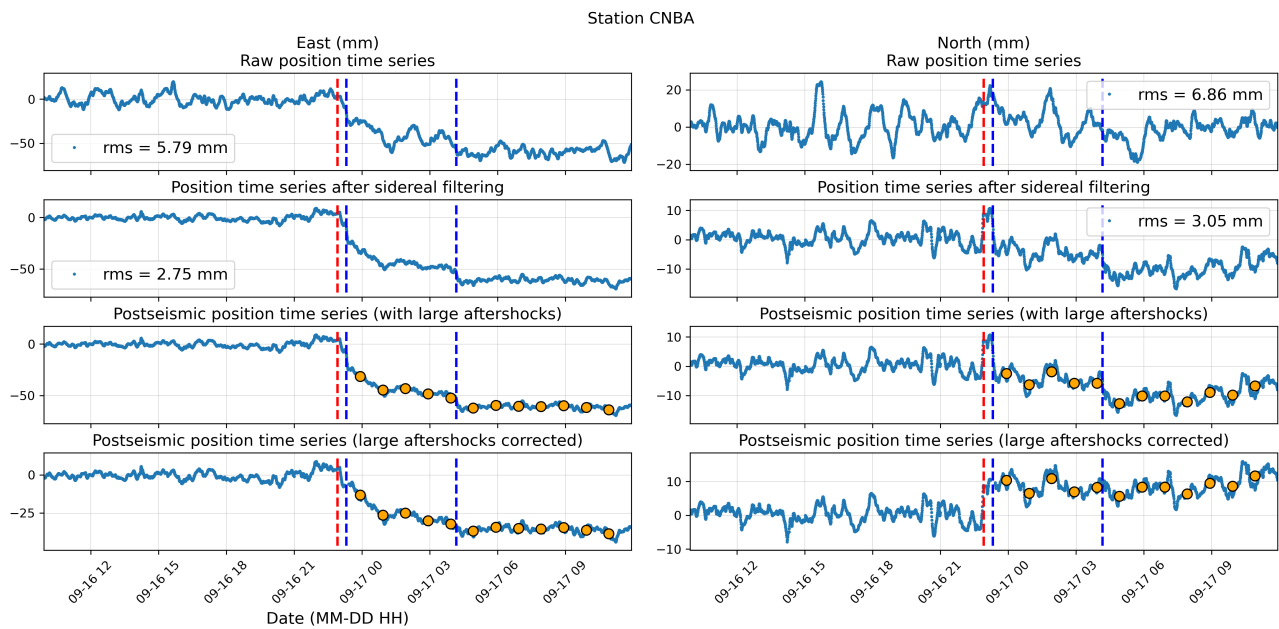


Figure S1.10.

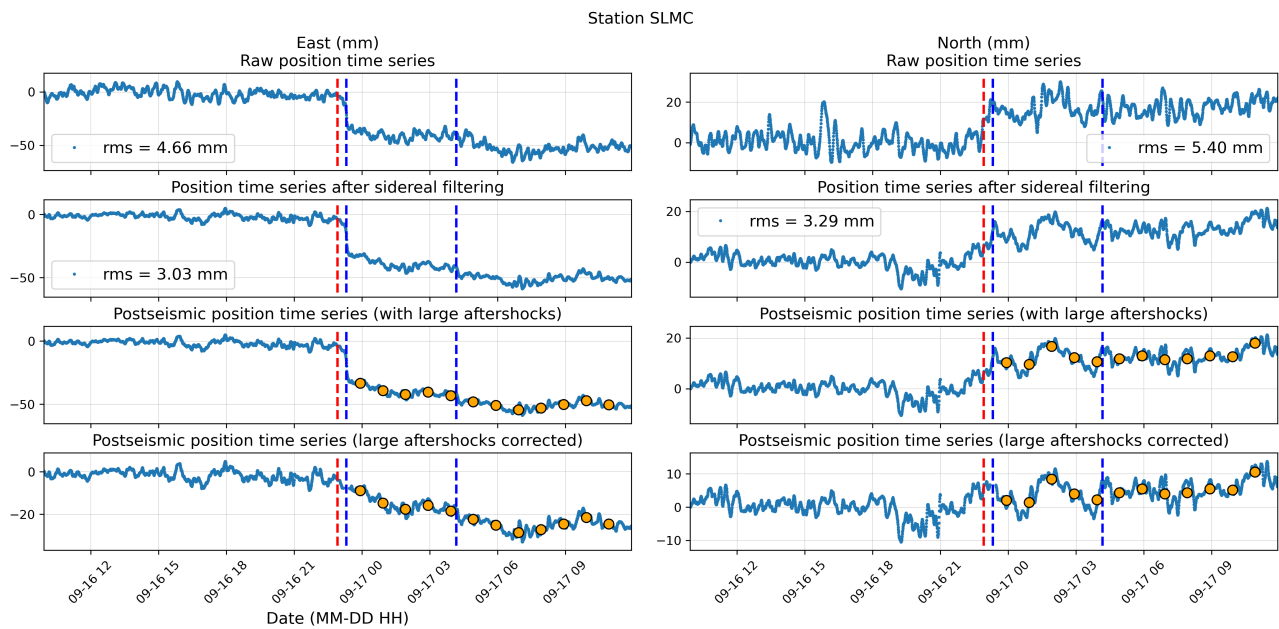


Figure S1.11.

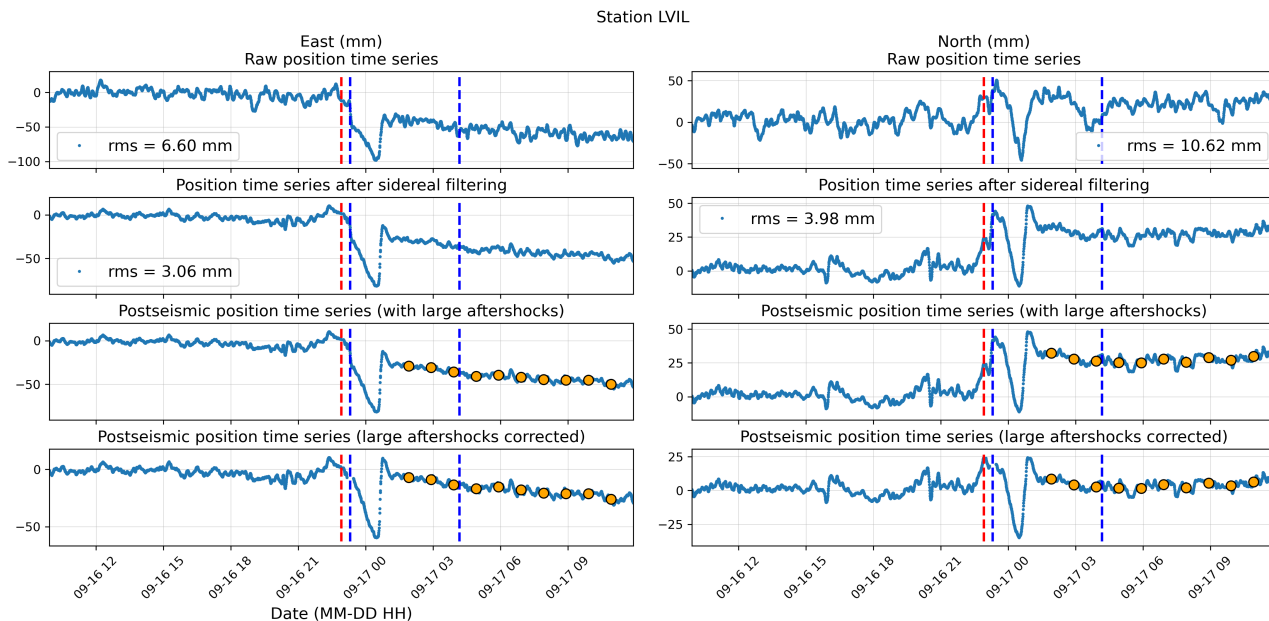


Figure S1.12.

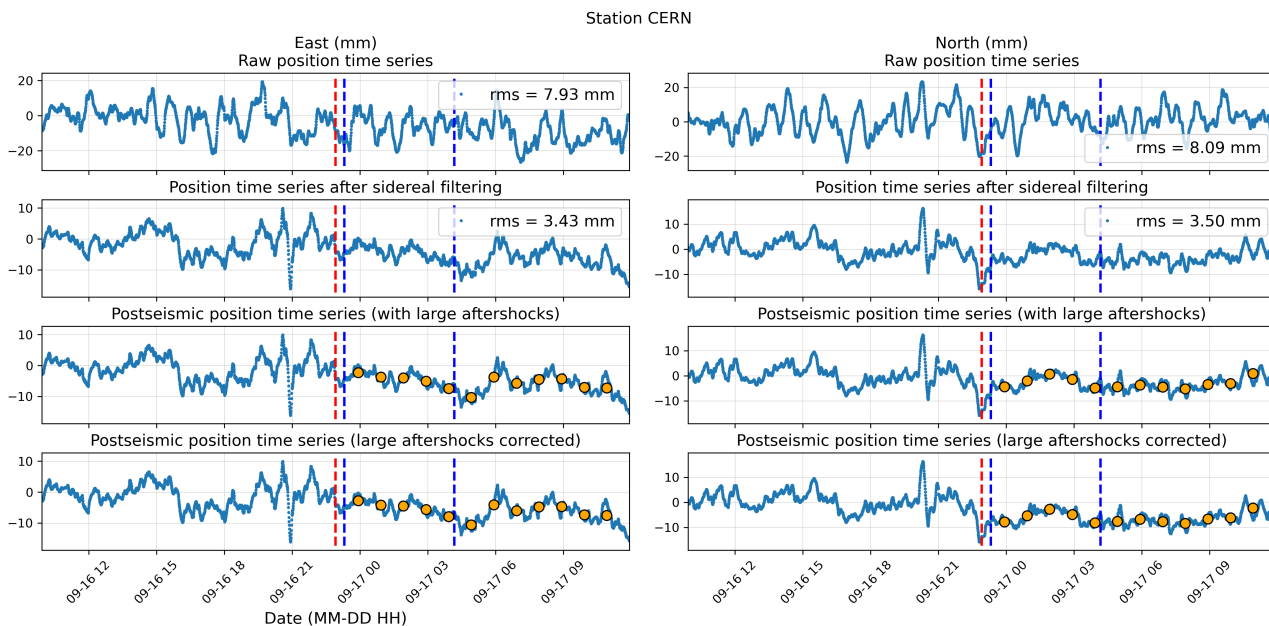


Figure S1.13.

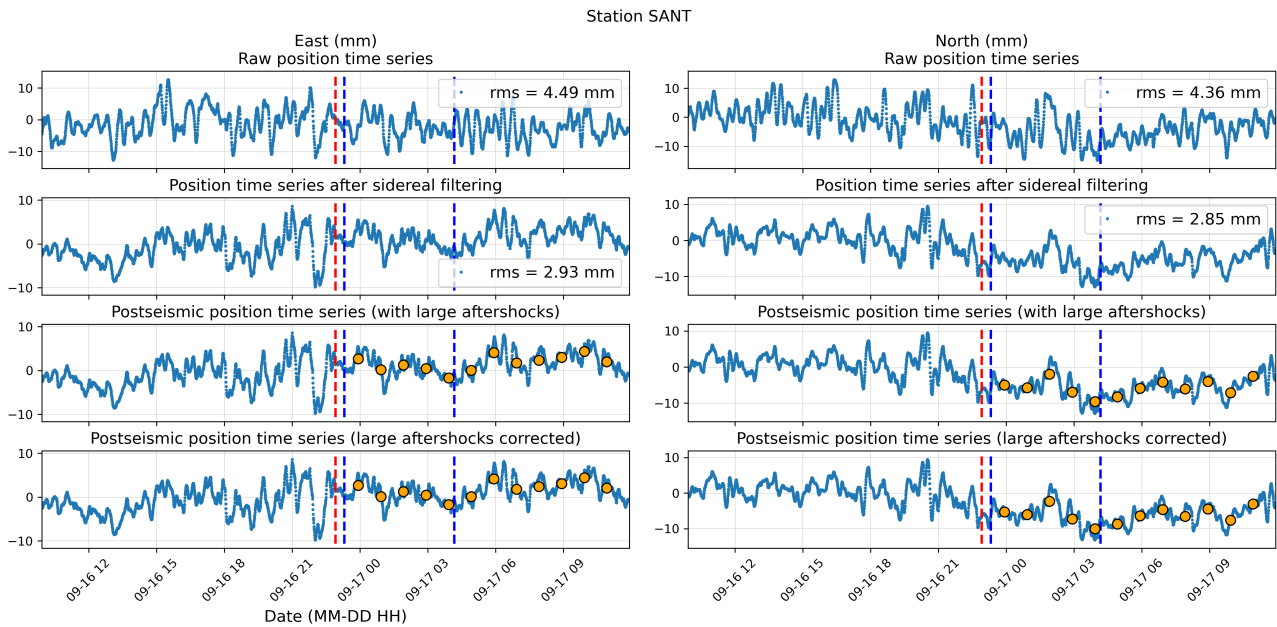


Figure S1.14.

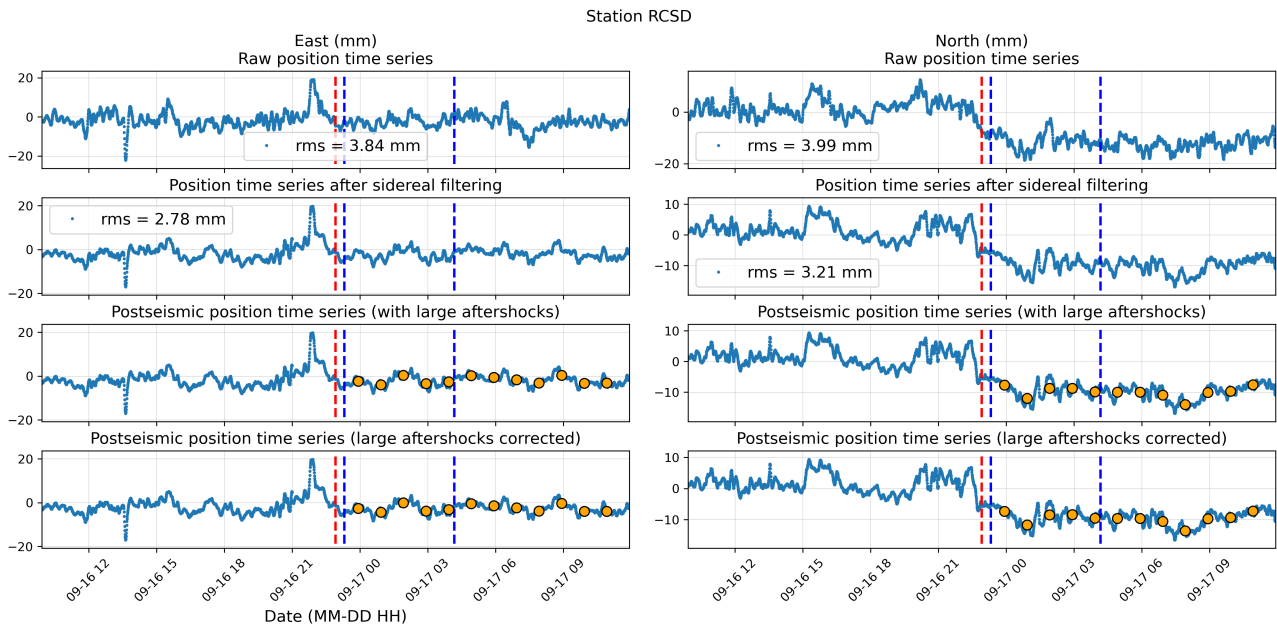


Figure S1.15.

S2 Choice of the smoothing parameter

As mentioned in the main text, the cost function has the following form:

$$\varepsilon = \frac{1}{N} \frac{\sum_{i=1}^N ((o_i - c_i)/e_i)^2}{\sum_{i=1}^N o_i^2} + \omega \Lambda \quad (1)$$

where N is the number of observations (2 horizontal components \times number of receivers), e is the error associated to the observation, Λ is the Laplacian of the slip distribution and ω is the weight given to the Laplacian. In order to choose ω we tested different values ranging from 1.0×10^{-6} and up to 1.0×10^6 . We use the L curve criterion to select the optimum value (Hansen, 1992). Based on the results shown in Figure S2.1 we choose 0.1 as the optimum value (red dot on Figure S2.1).

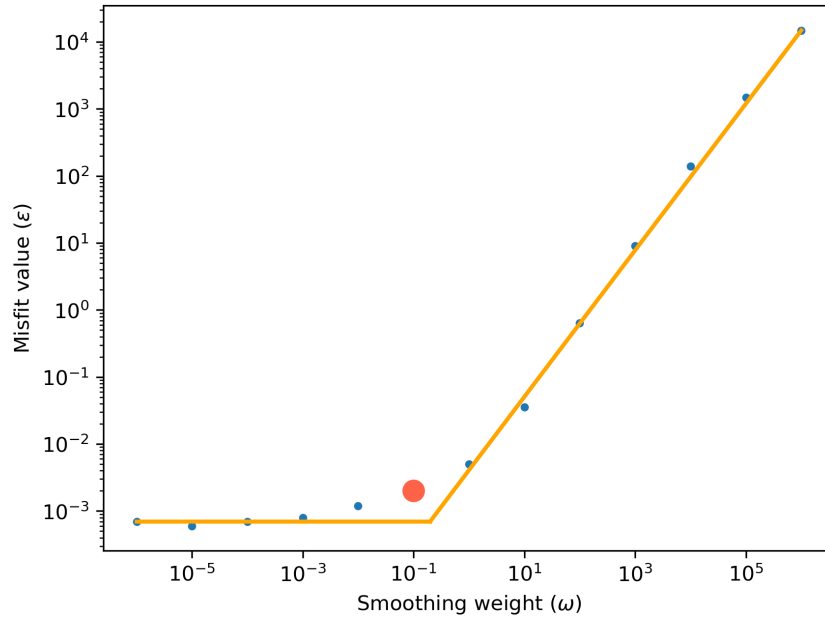


Figure S2.1.

S3 Comparison between observed and calculated surface displacements

In the following figures (Figure S3.1 to S3.15), we show a comparison between the observed position time series (blue) and the position time series calculated from the average post-seismic slip model (orange). Figure S3.16 shows a comparison between the observed and the calculated surface displacements in a map view at each time step.

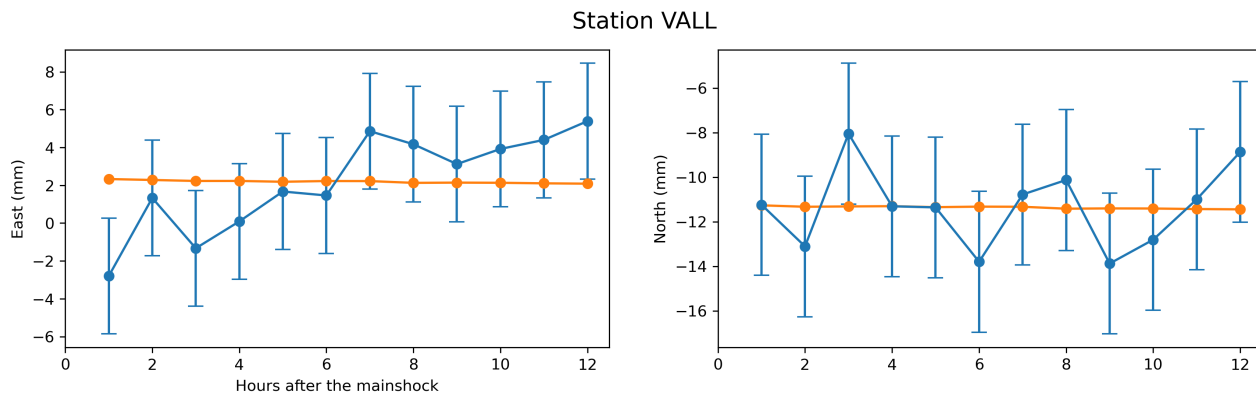


Figure S3.1.

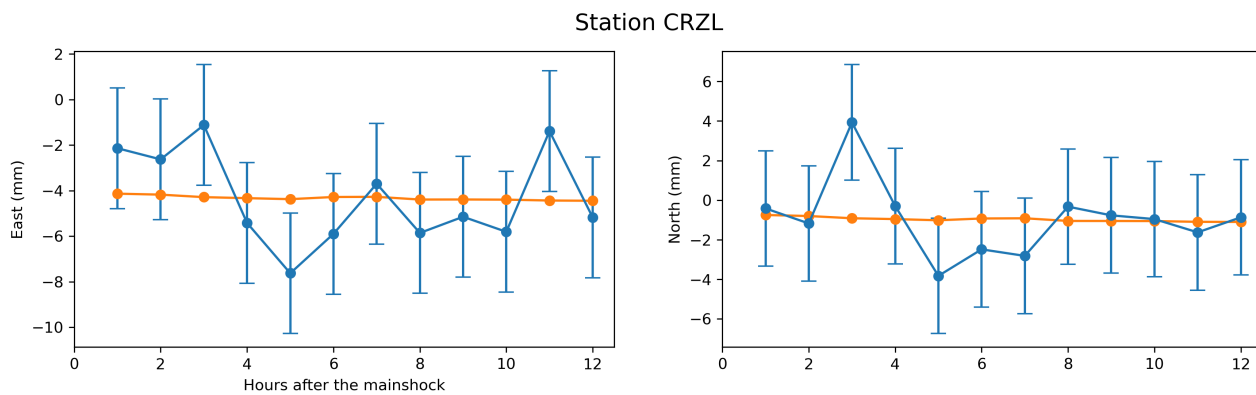


Figure S3.2.

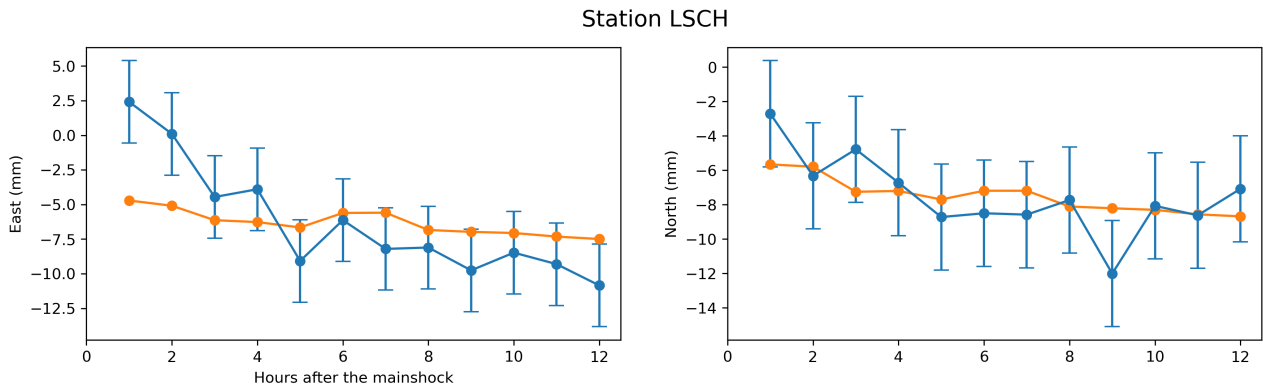


Figure S3.3.

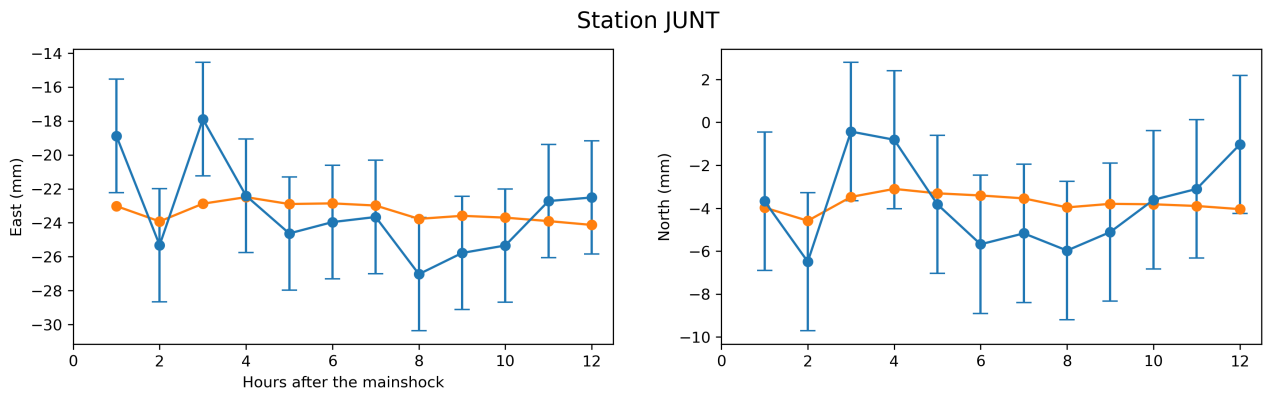


Figure S3.4.

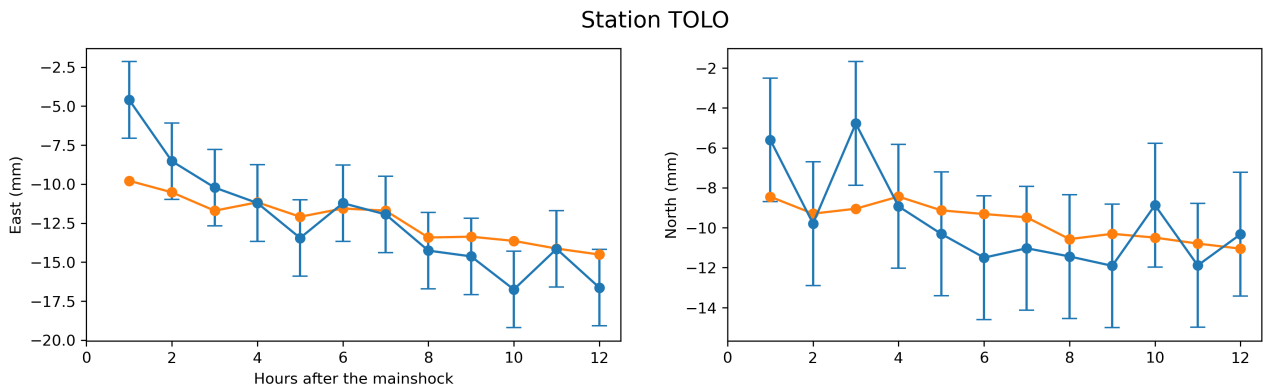


Figure S3.5.

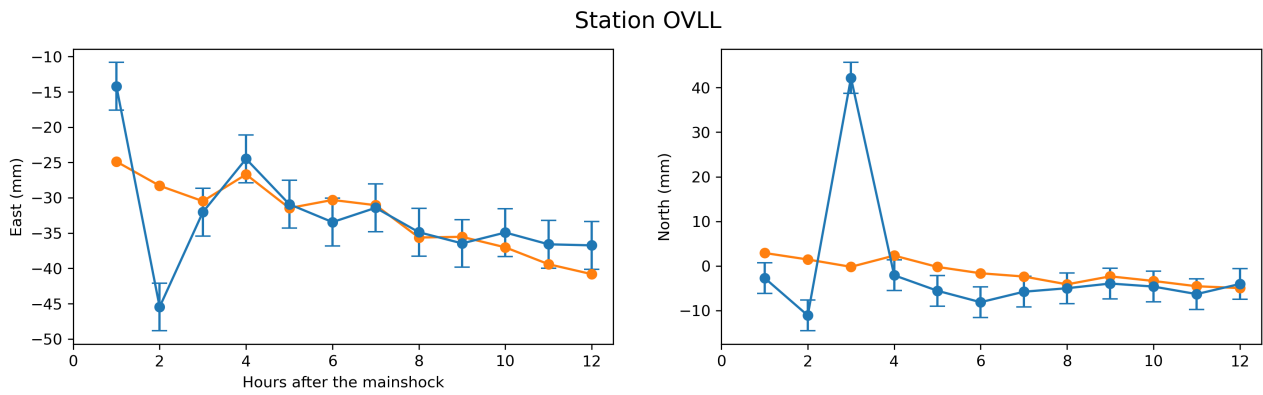


Figure S3.6. As mentioned in the main text, hours 2 and 3 at this station are disregarded during the inversion because the high-rate position time series show strong spurious signal that are not of tectonic origin, which consequently affect the averaging.

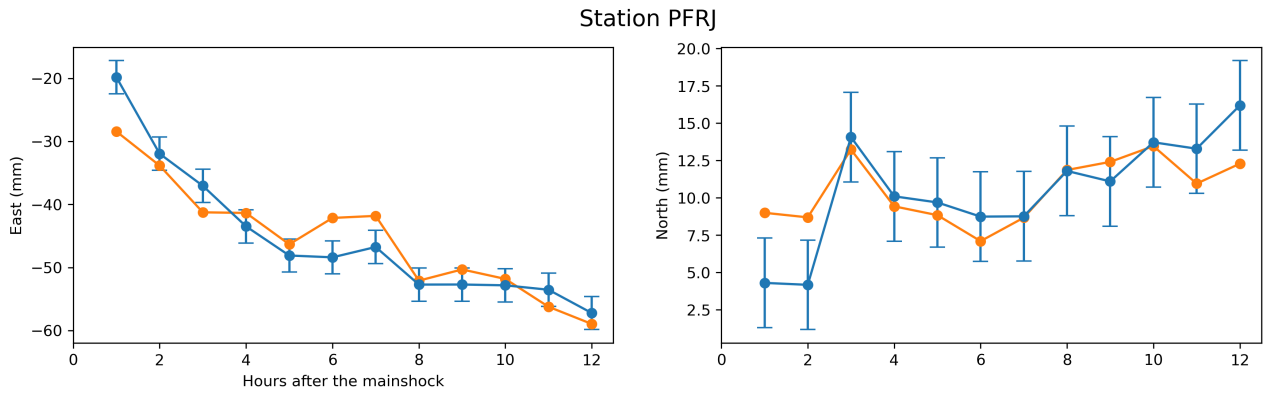


Figure S3.7.

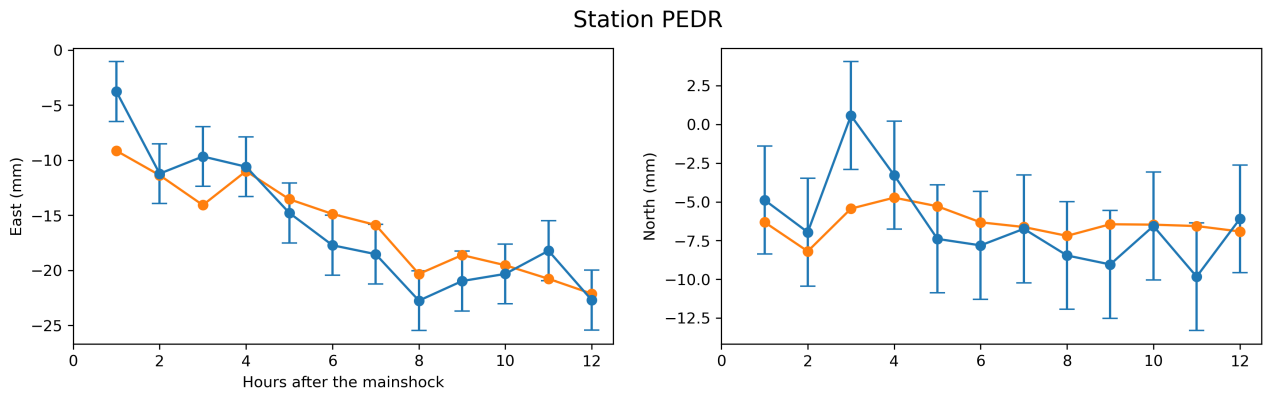


Figure S3.8.

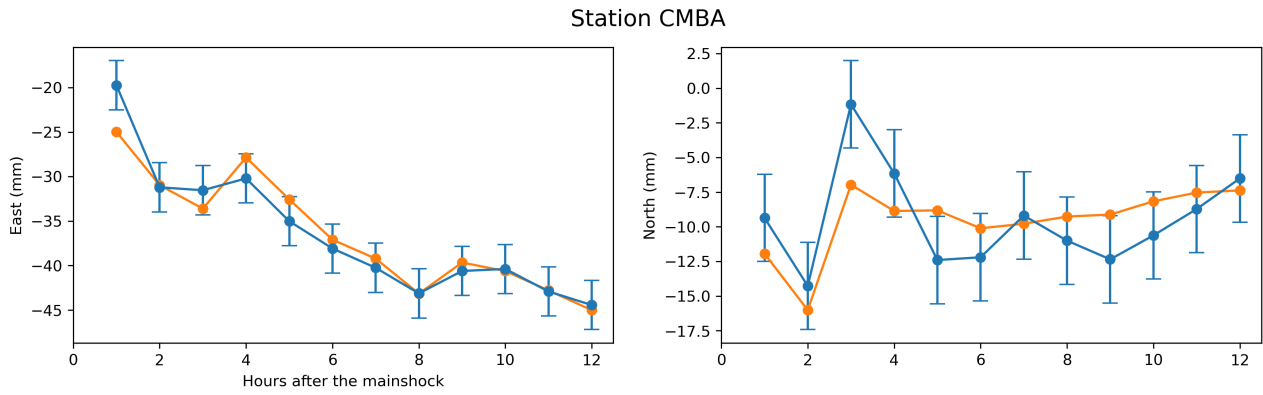


Figure S3.9.

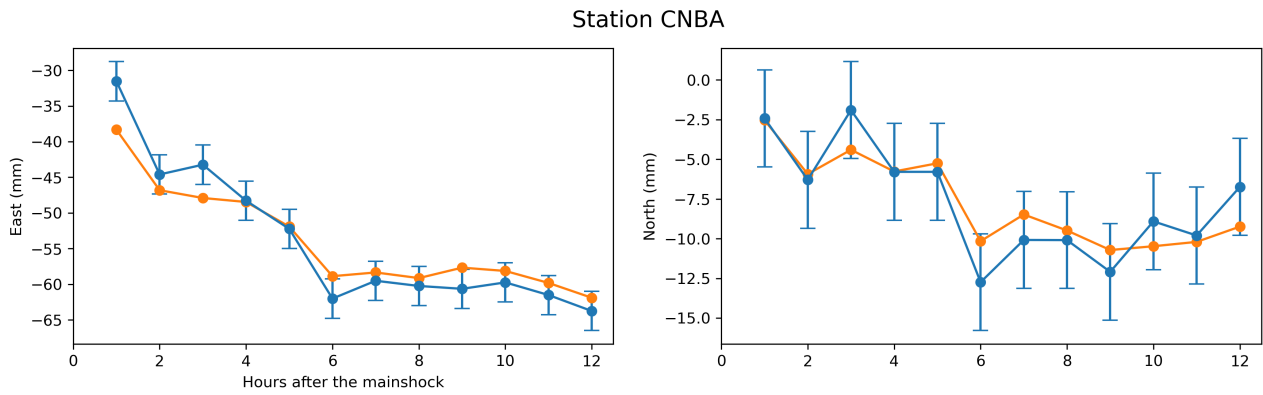


Figure S3.10.

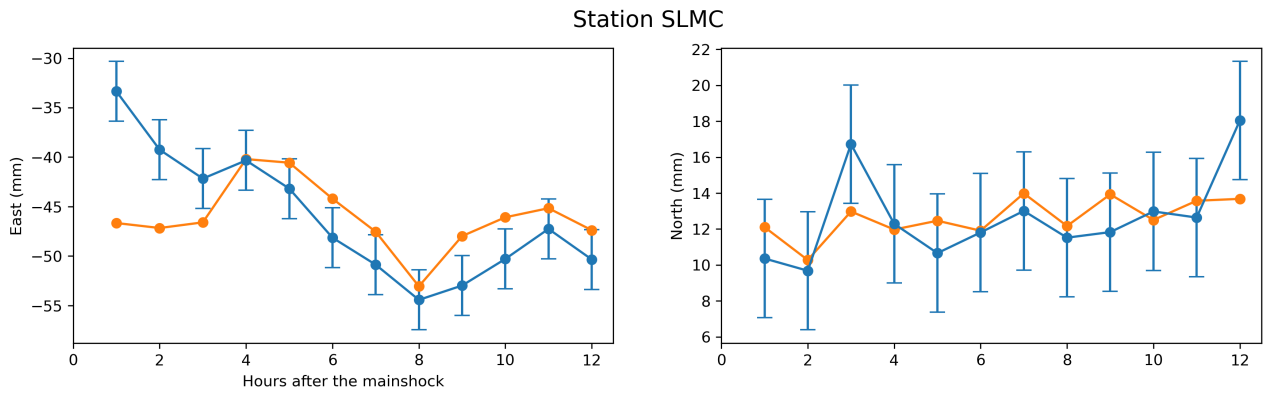


Figure S3.11.

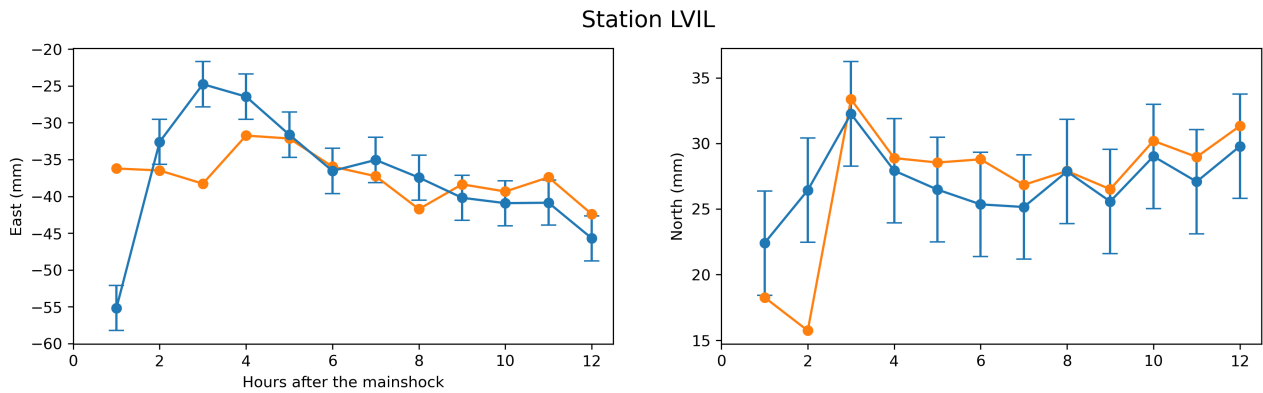


Figure S3.12. As mentioned in the main text, the first 2 hours at this station are disregarded during the inversion because the high-rate position time series show strong spurious signal that are not of tectonic origin, which consequently affect the averaging.

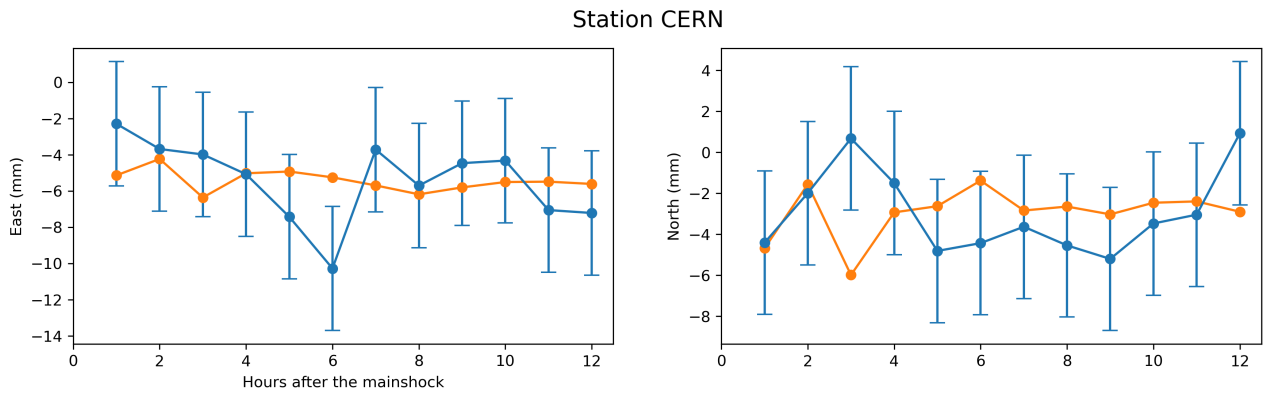


Figure S3.13.

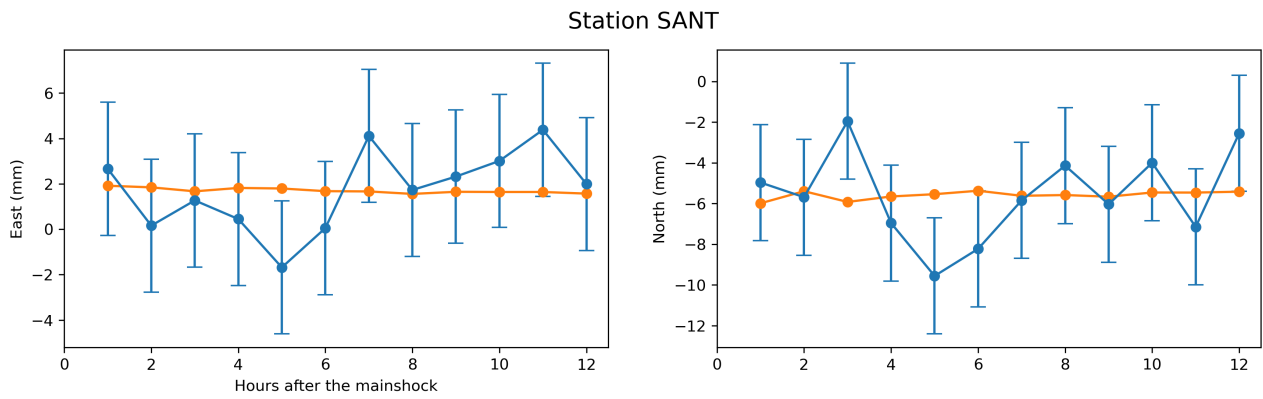


Figure S3.14.

Station RCSD

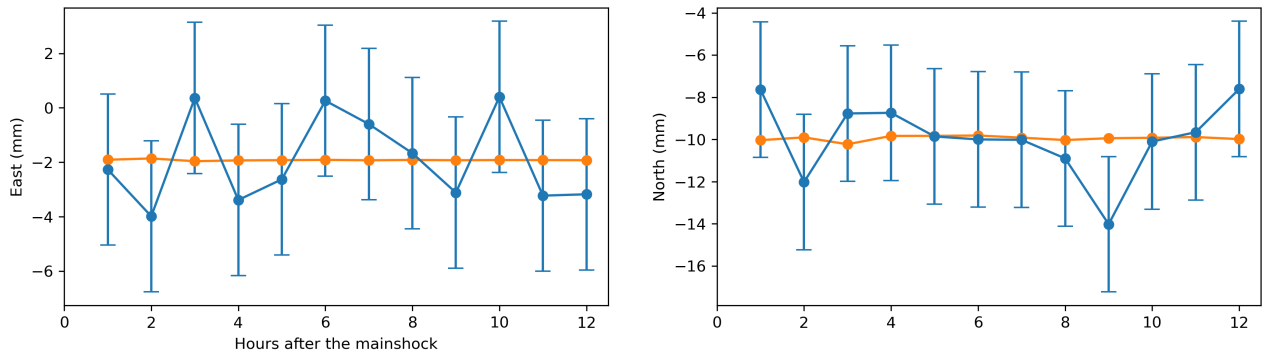


Figure S3.15.

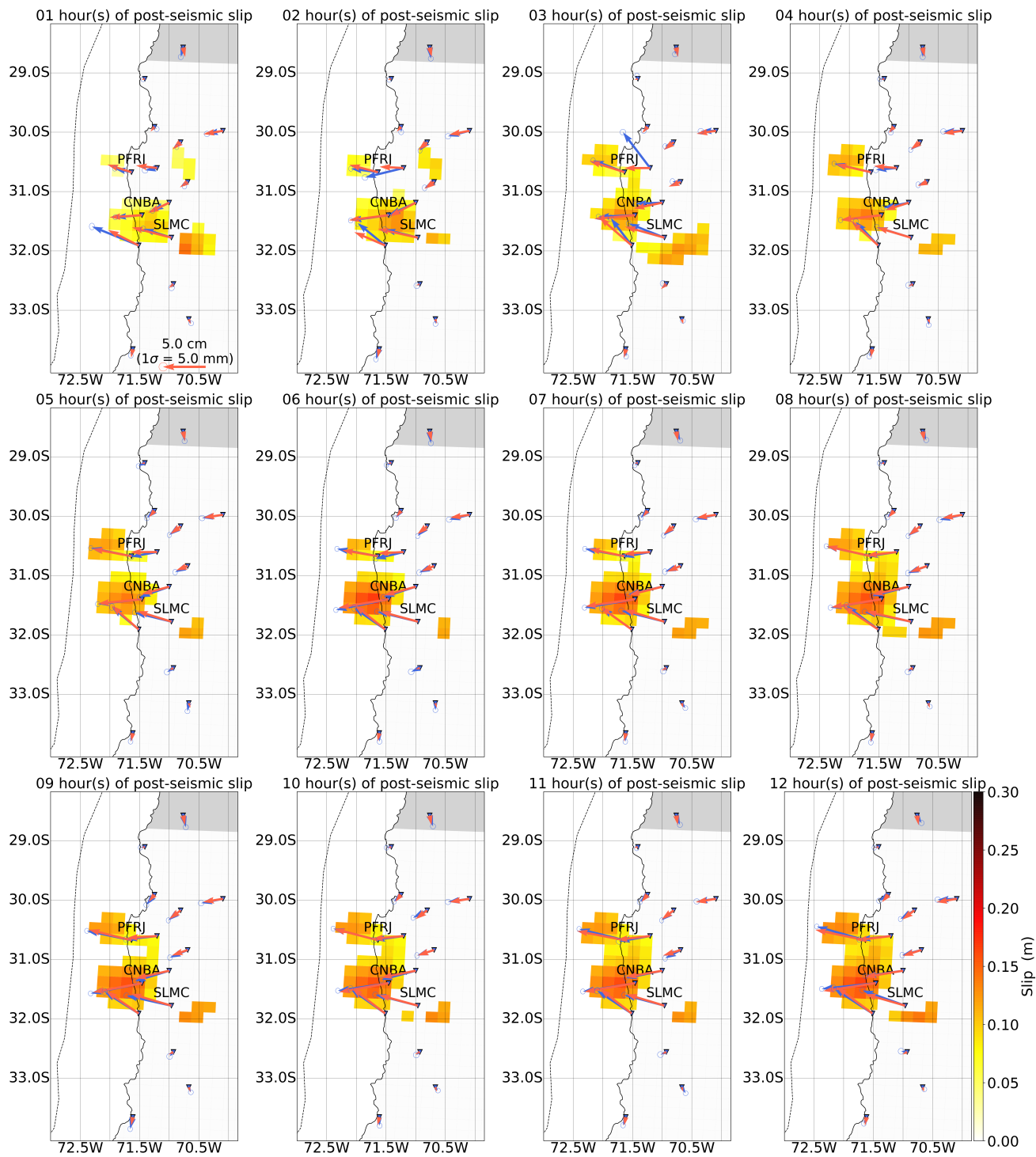


Figure S3.16.

S4 Comparison between the post-seismic slip model and various co-seismic slip models

Here, we compare the very-early post-seismic slip distribution after 12 hours with a non-exhaustive list of co-seismic rupture model from the literature (Figure S4.1). The model by Okuwaki et al. (2016) is the only one that is obtained using seismological data only (teleseismic waveforms). Thus, it is not at all contaminated by very-early afterslip. However, because only far-field data are used, it is likely that this model does not have the best resolution compared to the others. Melgar et al. (2016) uses the most complete dataset by including seismological data, tsunami data, high-rate GNSS data and InSAR data. Some contamination from very-early afterslip can be expected in the InSAR data since the tracks have been acquired 1 and 3 days after the mainshock. But, despite the fact InSAR data is used, most of the data are not contaminated by very-early post-seismic slip. Therefore, it is unlikely that the slip distribution contains a strong signature from the very-early post-seismic slip. This is why it has been chosen for the discussion in the main text. The model by Tillmann et al. (2015) is also obtained from a combination of seismological data and geodetic data (static offsets from GNSS data). Depending on the weighting adopted for each dataset, this model can be more or less affected by very-early post-seismic slip occurring during the first 12 hours. The remaining models presented are obtained using geodetic data only and are thus likely to be more or less contaminated by very-early afterslip. The model by (Shrivastava et al., 2016) is obtained using static co-seismic offsets measured from daily GNSS data. This is also the case for the model by (Ruiz et al., 2016). Then, the model by (Barnhart et al., 2016) is obtained by adding InSAR data. Finally, the co-seismic slip model obtained by Klein et al. (2017) comes from a combination of InSAR data, static co-seismic offsets from daily GNSS data and strict co-seismic offsets measured from high-rate GNSS data. Note that for almost all models, the 1-m slip contour is displayed on the figure (2-m for the model by Klein et al. (2017)).

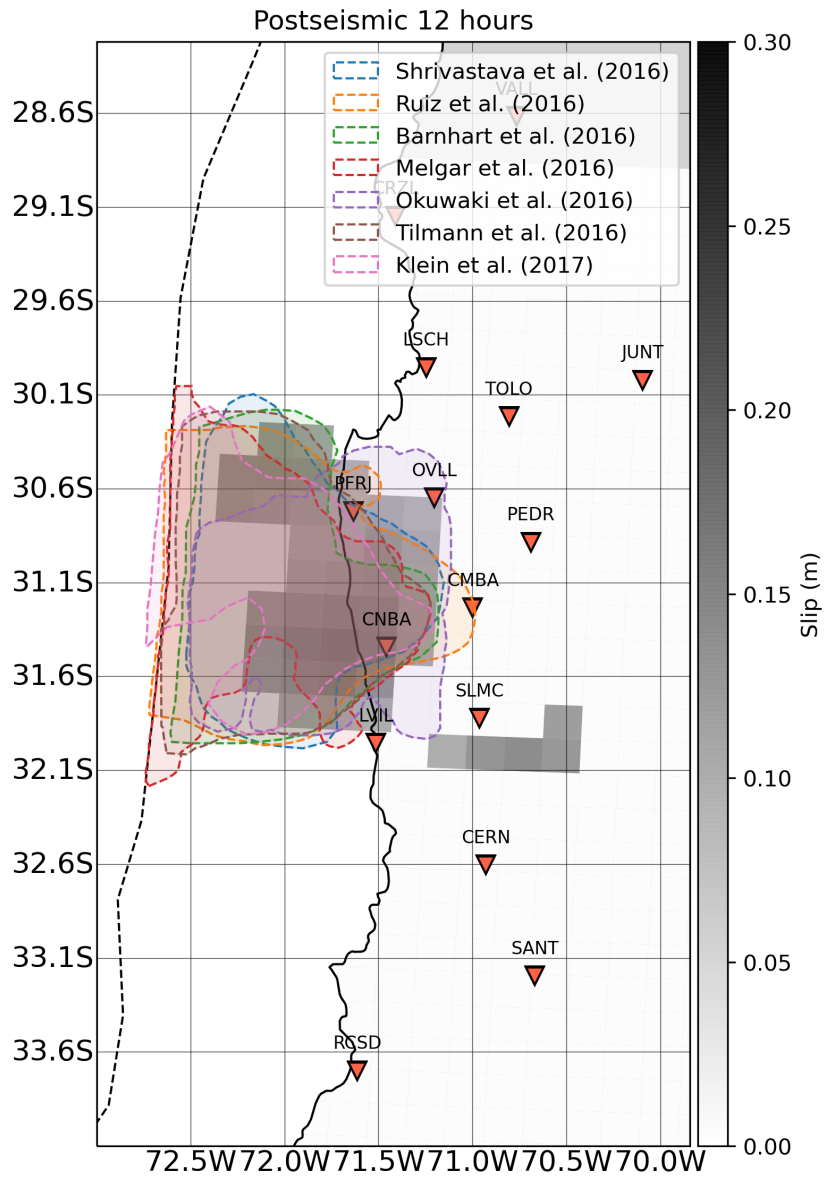


Figure S4.1.

50 S5 Sensitivity analysis

As mentioned in the main text, there is one area of deep post-seismic slip that is observed south-east of Salamanca (station SLMC - see Figure 3 in the main text). Here, we provide some evidences that, although it is significant in term of slip amplitude, it is an unreliable feature and its contribution to the surface displacements is negligible. First, we look at the standard deviation of the slip amplitude at each time step (Figure S5.1). It shows that the region south-east of SLMC always exhibits the largest level of uncertainty compared to the main regions of afterslip. This is the first indicator that this deep post-seismic slip is likely to be unreliable. It remains simply because its amplitude is larger than the standard deviation. However, as we will see next, even though this patch has a large slip amplitude, its contribution at the surface is negligible.

Next, we investigate the contribution of this patch by computing its response at the surface. We only show regions where the surface displacements are larger than the lowest noise level of all the observations combined (i.e., 2.45 mm).

60 When we look at the east component, we find that only LVIL and SLMC are affected. On the east component, the deep afterslip patch contributes at most to -6.0 mm and -4.2 mm of the modeled surface displacements for LVIL and SLMC, respectively. This is well below the observed and modeled surface displacements at these two stations (see Figure S3.12, Figure S3.11).

65 When we look at the north component, we find that only CERN and SLMC are affected. In this case, the deep afterslip patch contributes at most to 3.6 mm and -5.4 mm of the modeled surface displacements for SLMC and CERN, respectively. Thus, it is only for CERN that the contribution of this patch is significant with respect to the observed and modeled surface displacements (see Figure S3.13). But, we also note that at this station, the observed surface displacements barely exceed the noise level of the time series.

70 In conclusion, we find that the uncertainty level of this patch is higher than the main regions of post-seismic slip. In addition, we find that, regardless of the uncertainty level, the contribution of this patch to the calculated surface displacements is non-negligible only at station CERN, a station that exhibits almost no surface displacements. Therefore, based on these two lines of evidences, we conclude that this patch of deep post-seismic slip is not a reliable feature, which is why it is disregarded in the discussions in the main text.

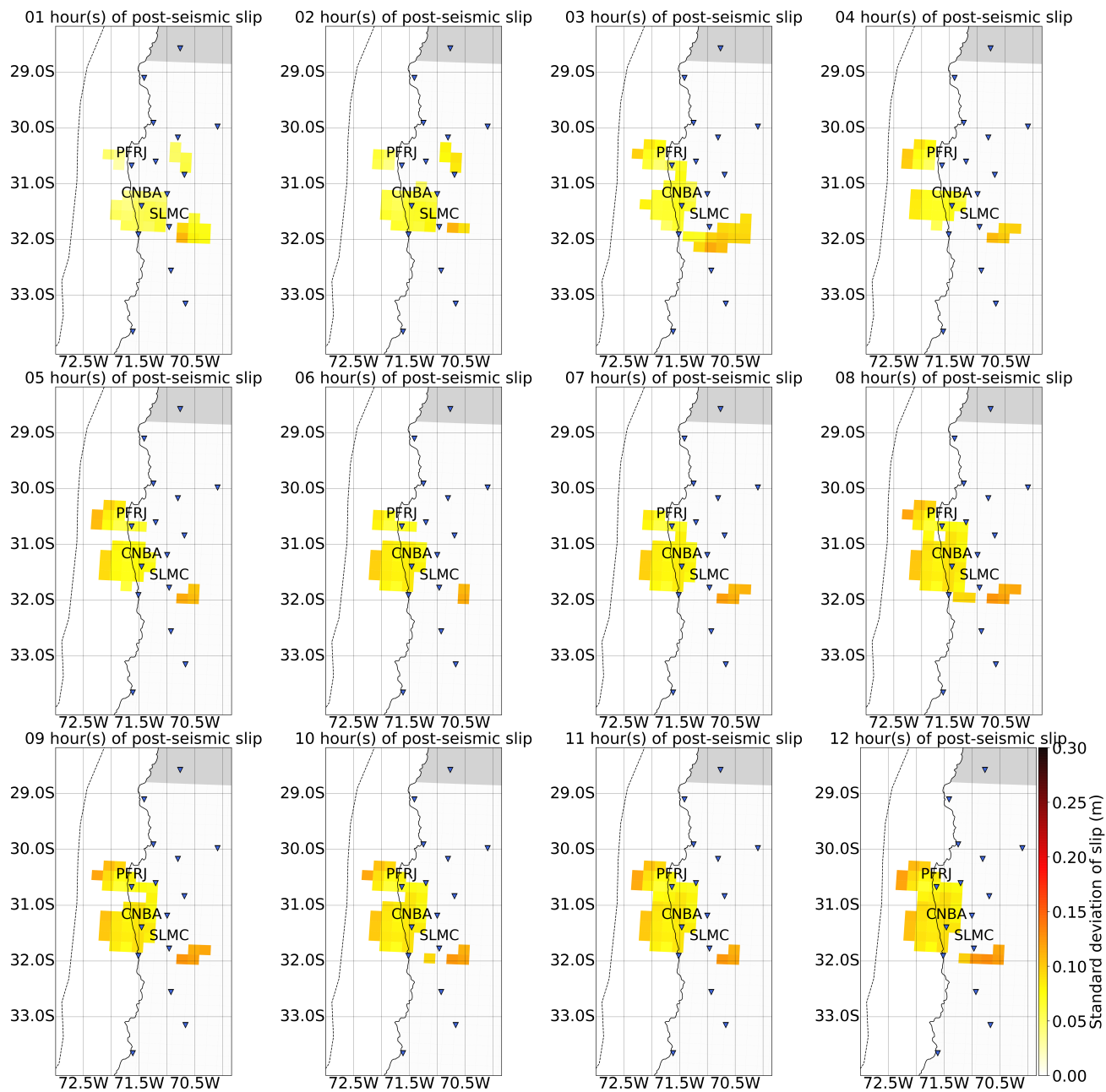


Figure S5.1.

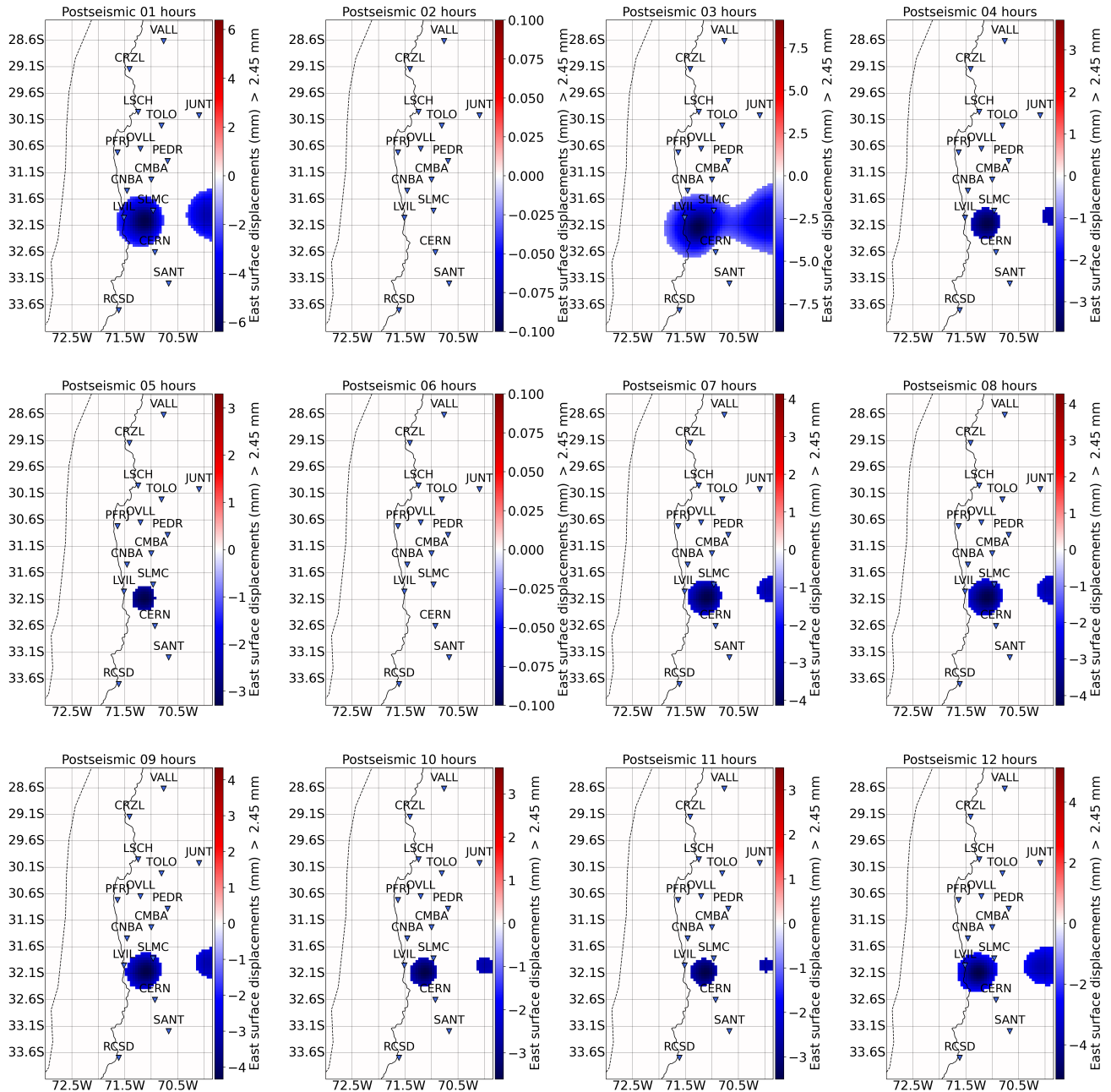


Figure S5.2.

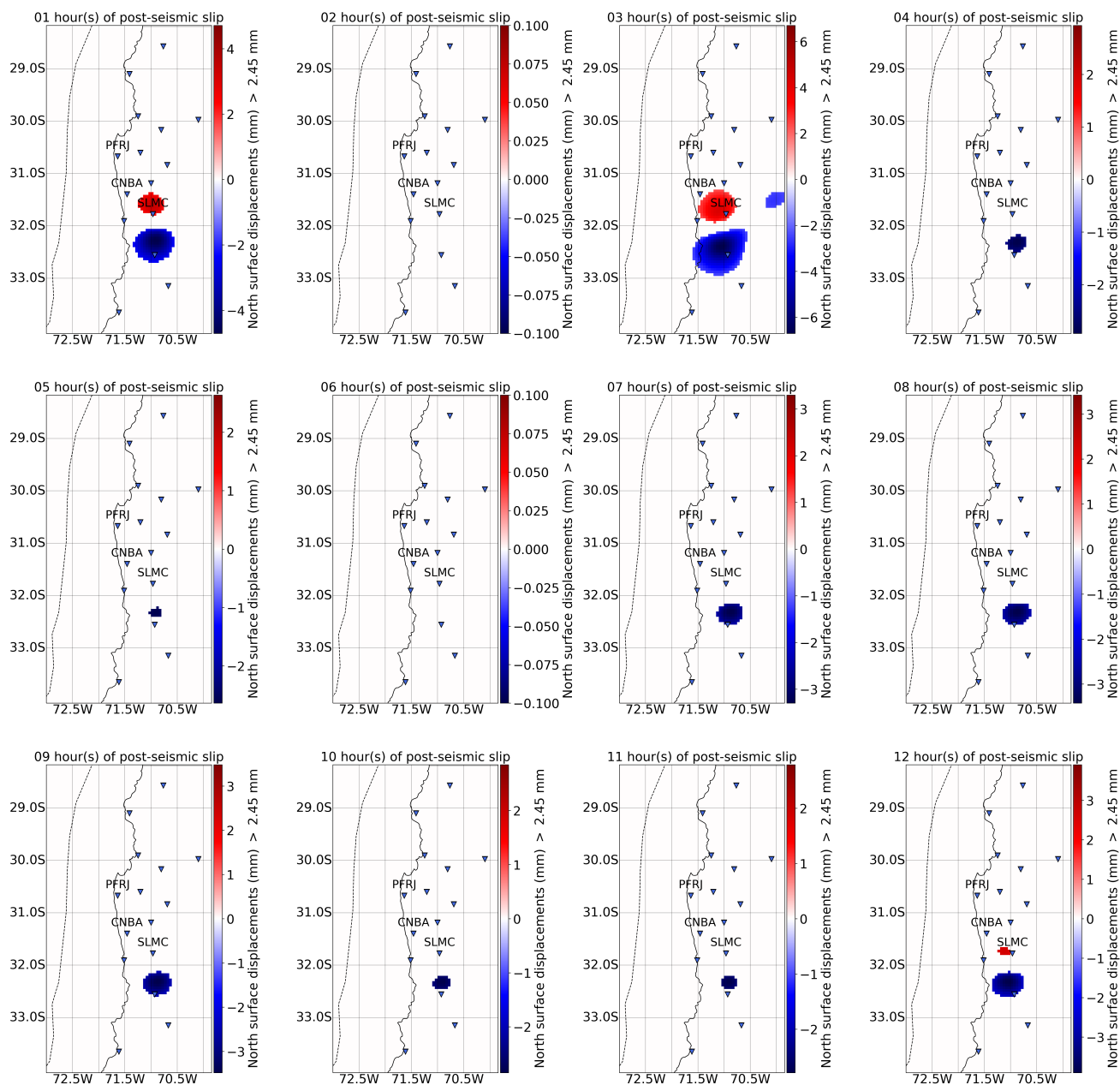


Figure S5.3.

S6 Comparison between very early post-seismic slip and very early aftershocks using Frank et al. (2017) catalog

- 75 In order to ensure that our conclusions are not strongly dependent on the chosen catalog, we also make a comparison between our post-seismic slip models and the catalog of aftershocks obtained from template-matching techniques by Frank et al. (2017). As shown by Figure S6.1, we observe an nearly identical pattern as what we observe using the catalog from Huang et al. (2017). Over the first 2 hours, most of the seismic activity occurs south of the rupture area, just as does the post-seismic slip. To the north, very little activity is seen during these first 2 hours but it then progressively intensifies just like the post-seismic slip.
- 80 After the first 12 hours of the post-seismic phase, we see a pattern where post-seismic slip and aftershocks strongly overlap, both surrounding the co-seismic rupture area.

Finally, we also compare the afterslip and aftershock temporal evolution using the aftershocks catalog from Frank et al. (2017) to ensure our conclusions about their relationship are not dependent of the catalog. We find the same relationship with the cumulative afterslip that relates with the log of cumulative number of aftershocks in the north patch (Figure S6.2).

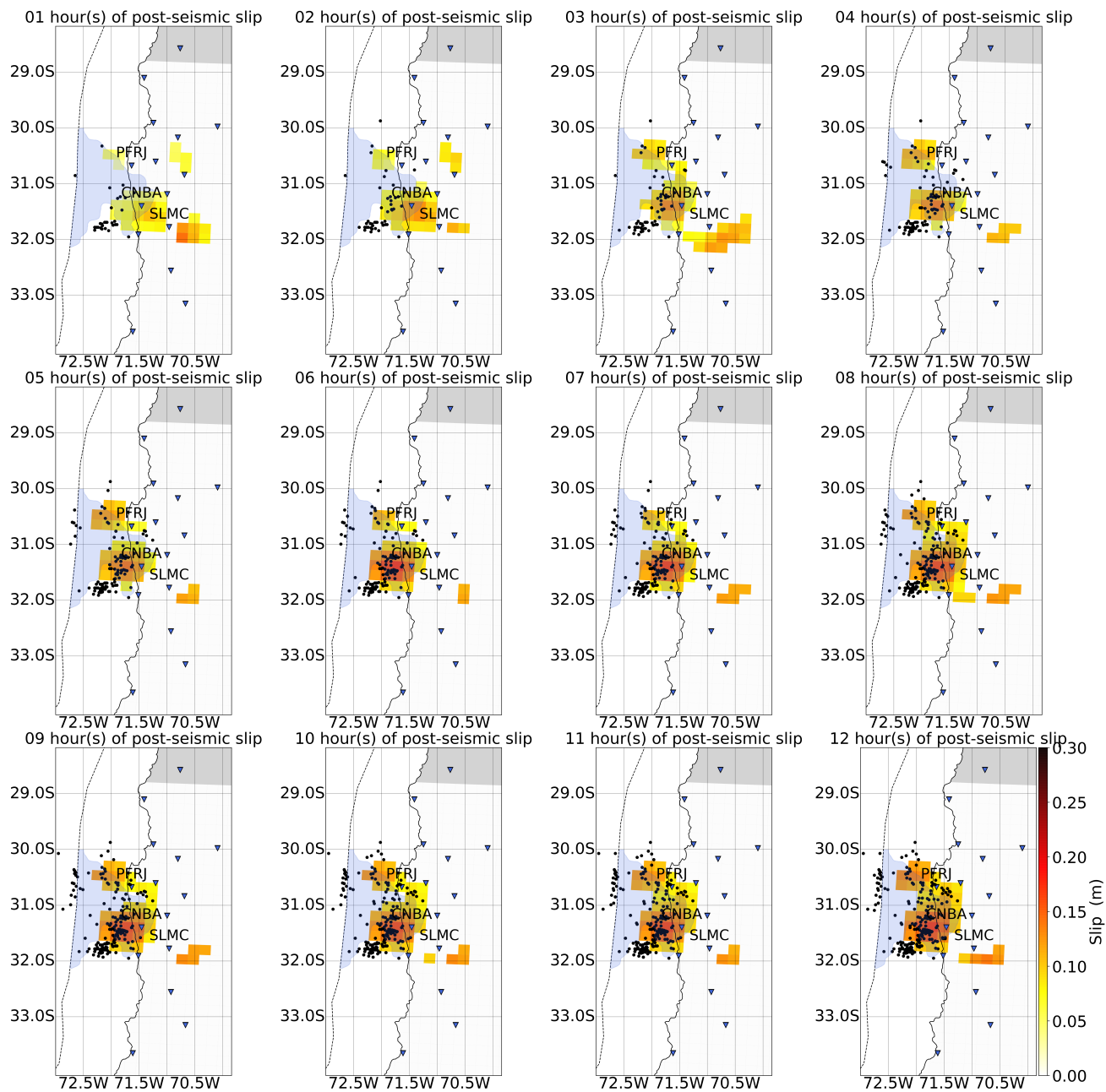


Figure S6.1.

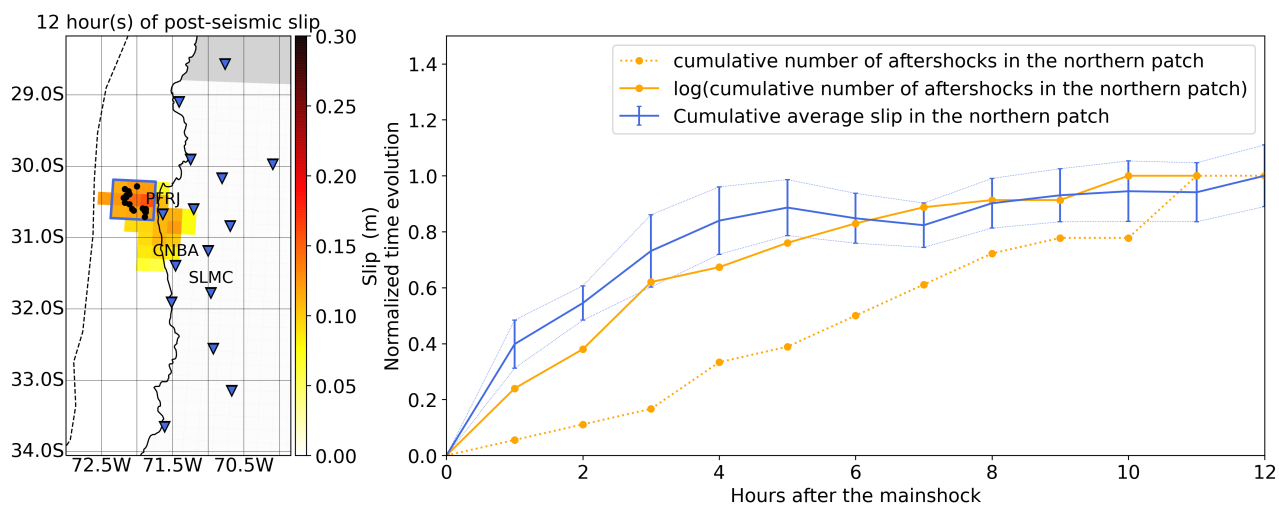


Figure S6.2.

85 S7 Comparison with the cumulative moment of aftershocks

As mentioned in the main text, we observe a bimodal frictional behavior during the very early post-seismic phase. We find that in the northern patch, slip is essentially aseismic slip while in the southern patch, slip is essentially seismic slip because of the aftershocks. We demonstrate it by imaging only the aseismic slip contribution of the post seismic slip, using the aftershock-corrected time series (see section 2.1 and 4.1). It could have also been inferred by comparing the time evolution of afterslip with the cumulative seismic moment from aftershocks in a given patch. When we do that, we clearly see that afterslip follows very well the cumulative moment from aftershocks in the south (Figure S7.1) while there is almost no correlation between the two in the northern patch (Figure S7.2). This is an additional indicator that slip in the southern patch is mostly seismic slip from the aftershocks while slip in the northern patch is largely aseismic slip.

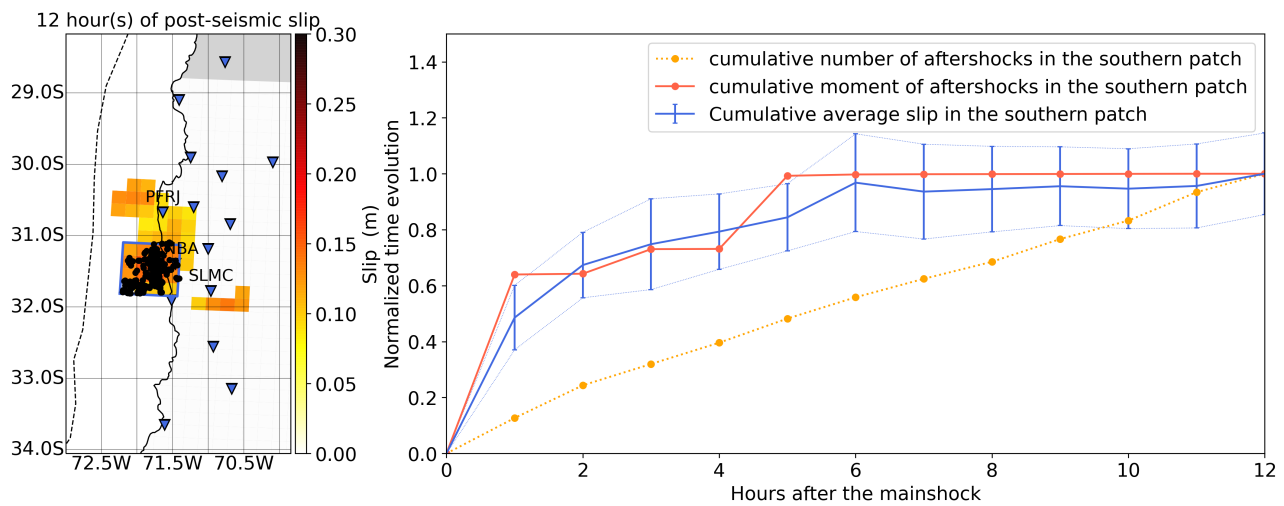


Figure S7.1.

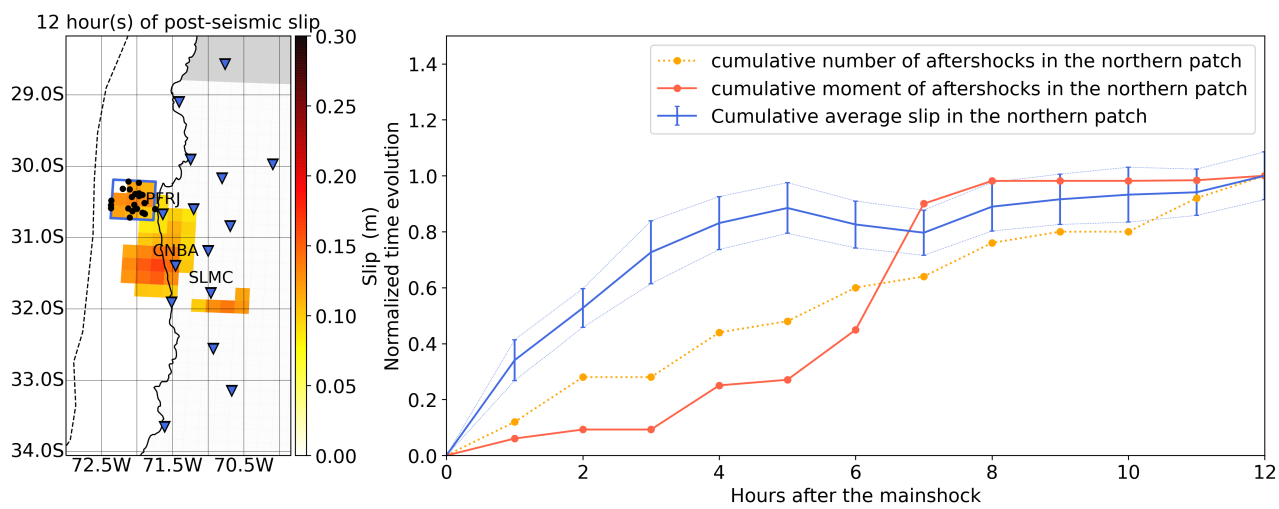


Figure S7.2.

References

- 95 Barnhart, W. D., Murray, J. R., Biggs, R. W., Gomez, F., Miles, C. P. J., Svarc, J., Riquelme, S., and Stressler, B. J.: Coseismic slip and early afterslip of the 2015 Illapel, Chile, earthquake: Implications for frictional heterogeneity and coastal uplift, *J. Geophys. Res. Solid Earth*, 121, 6172–6191, <https://doi.org/10.1002/2016JB013124>, 2016.
- Frank, W. B., Poli, P., and Perfettini, H.: Mapping the rheology of central Chile subduction zone with aftershocks, *Geophys. Res. Lett.*, 44, 5374–5382, <https://doi.org/10.1002/2016GL072288>, 2017.
- 100 Hansen, C.: Analysis of discrete ill-posed problems by means of the L-curve, *SIAM Rev.*, 34, 561–580, <https://doi.org/10.1137/1034115>, 1992.
- Huang, H., Xu, W., Meng, L., B urgmann, R., and Baez, J. C.: Early aftershocks and afterslip surrounding the 2015 Mw 8.4 Illapel rupture, *Earth Planet. Sci. Lett.*, 457, 282–291, <https://doi.org/10.1016/j.epsl.2016.09.055>, 2017.
- Klein, E., Vigny, C., Fleitout, L., Grandin, R., Jolivet, R., Rivera, E., and Metois, M.: A comprehensive analysis of the Illapel 2015 M_w 8.3 earthquake from GPS and InSAR data, *Earth Planet. Sci. Lett.*, 469, 123–134, <https://doi.org/10.1016/j.epsl.2017.04.010>, 2017.
- 105 Melgar, D., Fan, W., Riquelme, S., Geng, J., Liang, C., Fuentes, M., Vargas, G., Allen, R. M., Shearer, P. M., and Fielding, E.: Slip segmentation and slow rupture to the trench during the 2015 M_w 8.3 Illapel, Chile, earthquake, *Geophys. Res. Lett.*, 43, 961–966, <https://doi.org/10.1002/2015GL067369>, 2016.
- Okuwaki, R., Yagi, Y., Aranguiz, R., Gonzalez, R., and Gonzalez, G.: Rupture process during the 2015 Illapel, Chile earthquake: Zigzag-along-dip rupture episodes, *Pure Appl. Geophys.*, 173, 1011–1020, <https://doi.org/10.1007/s00024-016-1271-6>, 2016.
- 110 Ruiz, S., Klein, E., del Campo, F., Rivera, E., Poli, P., Metois, M., Vigny, C., Baez, J. C., Vargas, G., Leyton, F., Madariaga, R., and Fleitout, L.: The Seismic Sequence of the 16 September 2015 Mw 8.3 Illapel, Chile, Earthquake, *Seism. Res. Lett.*, 87, <https://doi.org/10.1785/0220150281>, 2016.
- Shrivastava, M. N., Gonzalez, G., Moreno, M., Chlieh, M., Salazar, P., Reddy, C. D., Baez, J. C., nez, G. Y., Gonzalez, J., and de la Llera, J. C.: Coseismic slip and afterslip of the 2015 M_w 8.3 Illapel (Chile) earthquake determined from continuous GPS data, *Geophys. Res. Lett.*, 43, 10710–10719, <https://doi.org/10.1002/2016GL070684>, 2016.
- 115 Tillmann, F., Zhang, Y., Moreno, M., Saul, J., Eckelmann, F., Palo, M., Deng, Z., Babeyko, A., Chen, K., Baez, J. C., Schurr, B., Wang, R., and Dahm, T.: The 2015 Illapel earthquake, central Chile: A type case for a characteristic earthquake ?, *Geophys. Res. Lett.*, 43, 574–583, <https://doi.org/10.1002/2015GL066963>, 2015.
- 120 Twardzik, C., Vergnolle, M., Sladen, A., and Avallone, A.: Unravelling the contribution of early postseismic deformation using sub-daily GNSS positioning, *Sci. Rep.*, 9, <https://doi.org/10.1038/s41598-019-39038-z>, 2019.